



CHORUS

This is the accepted manuscript made available via CHORUS. The article has been published as:

Molecular beam epitaxy of PdO on MgO (001)

Deshun Hong, Changjiang Liu, Linlin Wang, Jianguo Wen, John E. Pearson, and Anand
Bhattacharya

Phys. Rev. Materials **5**, 044205 — Published 29 April 2021

DOI: [10.1103/PhysRevMaterials.5.044205](https://doi.org/10.1103/PhysRevMaterials.5.044205)

Molecular beam epitaxy of PdO on MgO (001)

Deshun Hong¹, Changjiang Liu¹, Linlin Wang², Jianguo Wen³, John E. Pearson¹, & Anand Bhattacharya^{1#}

¹*Material Science Division, Argonne National Laboratory, Lemont, Illinois 60439, USA;*

²*Division of Materials Sciences and Engineering, Ames Laboratory, Ames, IA 50011, USA;*

³*Center for Nanoscale Materials, Argonne National Laboratory, Lemont, Illinois 60439, USA;*

PdO, widely used in catalysis in powder form for decades, has been predicted recently to be a Dirac semimetal. Synthesis of high-quality single crystals of this material is thus of great interest. Here, by using ozone-assisted molecular beam epitaxy, PdO thin films were grown on MgO (001) substrate. X-ray diffraction and transmission electron microscopy indicate the film is a/b axis oriented, with the c-axis lying in-plane. Fully oxygenated PdO films have a low density of hole-like carriers, and are insulating at the lowest temperatures. Our DFT calculations using the Heyd–Scuseria–Ernzerhof exchange-correlation functional suggest a ~ 1.0 eV band gap at the M-point, where the gap can be reduced by tensile strain along the c-axis and the bands begin to invert when the tensile strain is as high as 18%. Although tensile strain of this magnitude is experimentally not viable using epitaxy, electrons can be doped by oxygen reduction. Our results emphasize the need for careful consideration of electron correlation effects and stoichiometry in ab-initio modeling of topological semimetals involving transition metal oxides.

I. Introduction

As three-dimensional counterparts of graphene, Dirac semimetals (DSMs) host massless Dirac fermions with 3D linear dispersion around Dirac nodes [1]. These Dirac nodes are formed due to band inversion and are protected by time reversal and crystalline symmetries. DSMs can be viewed as intermediate states between topological insulators and normal insulators, both of which have a bulk band gap [2-3]. In DSMs, each node is 4-fold degenerate. Either time reversal or inversion symmetry breaking will lift the band degeneracy, and a Dirac node will become a pair of 2-fold Weyl nodes, which can be viewed as source or sink of magnetic flux in reciprocal space [4]. Various interesting behaviors have been reported in topological semimetals including anomalous magneto-transport [5-8] and giant spin to charge conversion efficiency [9-12]. Searching for new topological semimetals and the realization of topological phase transitions are thus of great current interest.

Although many topological semimetals (TSMs) have been predicted and several have been realized, materials with topological nodes closer to the Fermi surface, with longer Fermi arcs to realize more robust topological properties, and where there is minimal interference from carriers from topologically trivial bands, are rare and much sought after. Thus, there is an extensive search for topologically robust and chemically stable TSMs. Starting from symmetry considerations and supported by theoretical calculations, several topological material databases now serve as guides for experimentalist [13-15] seeking to synthesize new topological materials. On the experimental front, Na₃Bi [16] and Cd₃As₂ [17] whose Dirac nodes are situated very close to the Fermi level are two good examples of DSMs realized

in the lab. However, these two materials are not chemically stable in ambient conditions, a factor that hinders their use in applications. Oxides that may be chemically more stable and topologically nontrivial are thus of significant interest.

PdO which crystallizes in tetragonal structure with space group of $P 4_2/m m c$ (131), has been predicted to host Dirac fermions, and its topological properties are protected by 4-fold rotational symmetry along c axis [15]. According to density functional theory (DFT) calculation [18-19] using modified Becke–Johnson (mBJ) potential [20-21], there is a band inversion near the M -point [15] and the Dirac nodes are very close to the Fermi level which makes PdO an ideal candidate for device applications. Synthesis of high quality PdO crystals would be of great interest in order to investigate these properties.

PdO has been widely used for gas detection as well as catalysis in the form of polycrystals [22-23] and in fact polycrystalline PdO thin films have been synthesized by post-annealing Pd film in oxygen [24-26]. In this work, we grew a/b oriented crystalline PdO thin films on MgO (001) by ozone assisted molecular beam epitaxy (O₃-MBE). Structure and transport properties of the films were characterized, and we also calculated the electronic structure using DFT with Heyd–Scuseria–Ernzerhof (HSE) [27] exchange-correlation functionals to better understand the role of correlations.

II. Growth and Diffraction

The structure of PdO is shown in the bottom inset of Fig. 1a, where each unit cell is composed of Pd and O layers alternatively stacking along the c -axis. With a tetragonal structure, the PdO lattice constants a and c are 3.060 Å and 5.372 Å respectively [28]. We synthesized PdO thin films using O₃-MBE on (001) oriented MgO substrate by evaporating Pd at 1450 °C using a high-temperature effusion cell, with growth rate of 0.5 Å/min which is calibrated by a quartz crystal microbalance (QCM). To mitigate the formation of oxygen vacancies, pure distilled ozone was delivered through a nozzle toward the substrate during the growth, where the pressure was maintained at 3×10^{-6} Torr using a 1500 liters/s turbo pump. The substrate was held at a temperature of 200 °C during growth. The surface crystal structure was monitored by in-situ reflection high energy electron diffraction (RHEED) with 10 kV acceleration voltage. Before growth, MgO substrates were cleaned by sonicating in acetone & isopropyl alcohol and further annealed in ozone (1×10^{-6} Torr) at 600 °C for 1 hour to improve the surface quality. As can be seen in the top inset of Fig. 1a, RHEED images before (up) and after (down) growth were obtained. After growth, a streaky pattern can be clearly seen, indicating high crystallinity as well as flat surface morphology of the film. Furthermore, there are two sets of streaks according to the spacing, as indicated by yellow and red arrows in the RHEED image. The ratio between these two spacings is ~ 1.77 , close to $c/a \sim 1.76$ in bulk, which will be discussed later. The flatness of PdO film was further confirmed by X-ray reflectivity (XRR) using Cu $K_{\alpha 1}$ radiation in Fig. 1a. Single period fringes in the XRR appear over the entire measured 2θ range which suggest a sharp interface as well as small roughness of the sample. By fitting to a model constraining the densities of MgO and PdO to 3.58 g/cm³ and 7.76 g/cm³ respectively, a thickness of 15.8 nm in PdO film is obtained, while the roughness of PdO surface and the MgO/PdO interface 2.5 Å and 1.0 Å respectively. Crystal structure and film morphology were further

characterized by X-ray diffraction (XRD) and atomic force microscopy (AFM), as shown in Fig. 1b. Root mean square (RMS) roughness of the film is ~ 0.3 nm in 500 nm x 500 nm range, consistent with XRR fitting. Interestingly, tweed-like textures along diagonal [110] directions can be clearly seen, which is due to strain relaxation, and are an indication of twinning of the film on the MgO substrate as we will discuss later. Our XRD measurements show that the film is [100] / [010] oriented, which means the c -axis of the tetragonal structure lies in the MgO (001) plane. The position of (100) peak at 29.27° gives lattice constant of 3.05 \AA for a/b , close to 3.06 \AA in bulk. For the PdO (200) peak where $2\theta = 60.68^\circ$, the full width at half maximum (FWHM) is 0.64° , which gives 15.9 nm *out-of-plane* domain size on average according to Sherrer equation $\tau = \frac{K\lambda}{\beta \cos\theta}$ [29] (τ is the domain size, K is the shape factor that close to unity (we use 1 in the estimation) and β is the FWHM of 2θ). This domain size is nearly equivalent to the film thickness (15.8 nm) which suggest the film is highly ordered *out-of-plane*.

To further check the PdO's epitaxial relation with MgO substrate, we carried out azimuthal scans by rotating along [001] direction of substrate, while aligned to MgO {111} and PdO {110} peaks, as can be seen in Fig. 2a. Although a 90° period was expected from the MgO substrate, a 4-fold symmetry for PdO {110} peaks is surprising at first glance (PdO should be 2-fold symmetric in this if the c -axis lies in the (001) plane of MgO). The most likely reason of the measured 4-fold symmetry is that the film is twinned, as is also suggested by our AFM measurements. Since the PdO c -axis can orient along two equivalent diagonal directions in MgO (001) plane, the 4-fold symmetry around PdO {110} as well as its alignment with MgO {111} can be explained. When viewing along [110] direction of MgO, both ab and ac planes of PdO can be seen. This is consistent with two sets of RHEED streaks mentioned above. By considering both *out-of-plane* and *in-plane* XRD measurement, the epitaxial schematics are shown in Fig. 2b. The c -axis of PdO is oriented along the diagonal direction [110] / [$1\bar{1}0$] of MgO substrate. For simplicity, only one of the twins is shown. The other one can be obtained by a 90° rotation in the MgO (001) plane.

III. TEM Characterization

Transmission electron microscopy (TEM) is a direct technique to characterize the crystal structure at atomic level. For twinned structures, two kinds of atomic structures should be directly visible along certain directions in TEM images. Here, we cut the sample in one diagonal direction [110] of the substrate and view along the perpendicular direction [$1\bar{1}0$]. To minimize induced defects during TEM sample preparation, the film was mechanically polished, thinned by low energy Ar^+ ion milling at 4 kV, and finally polished at 0.2 kV. As discussed above, atomic structure along both ab and ac planes should be directly seen when viewing diagonally. Aberration-corrected high-resolution transmission electron microscopic (HRTEM) images as well as Fast Fourier Transform (FFT) patterns can be seen in Fig. 3 where both images show sharp interfaces and highly ordered atomic structures. There are two kinds of atomic configurations: rectangle and square which correspond to ac and ab respectively. By calculating the lattice constant of ac plane (Fig. 3a) and ab plane (Fig. 3b) (using MgO atomic spacing as an internal reference), we get $a \sim 3.04 \text{ \AA}$ and $c \sim 5.34 \text{ \AA}$, consistent with the values we get from XRD and RHEED, and the film turns out to be fully relaxed.

Considering the lattice constant of the cubic MgO, the minimum lattice mismatches are 2.5% and -10% for PdO a and c , which are not small for oxides and the film relaxes soon after the first few layers. This relaxation can be visually inferred from AFM result in Fig. 1c that show dense grain boundaries aligned along two diagonal directions. Before the growth, our primary assumption was that the PdO film would be c -axis oriented with a/b directions in plane since the mismatch is 2.5% only, which turns out to not be the case in the actual growths. This suggests the PdO growth on MgO may be constrained by surface energy. We point out that along the c -axis in PdO, alternative stacking of Pd²⁺ and O²⁻ layers is polar with high surface energy, while along the a/b directions each termination layer is charge-neutral and possibly more favorable for film growth.

IV. Transport and DFT Calculation

Recent theoretical work on searching for topological materials by considering symmetry indicators in non-magnetic materials [15] suggests that PdO might be a Dirac semimetal, with Dirac nodes near the M point in the Brillouin zone and very close to the Fermi level. This can be checked by measuring transport properties. Here, we sputtered 100 nm Pt (some devices using Ti-Au) electrodes and measured the temperature dependence of resistivity of our films in a Van der Pauw geometry. As can be seen in Fig. 4a, the film shows insulating behavior at low temperatures. However, the relatively low resistivity even at low temperatures ($< 1\Omega\cdot\text{cm}$) suggests conduction via shallow defect states. We fitted the measured curve using the expression for hopping conduction $\rho = \rho_0 e^{\left(\frac{T_0}{T}\right)^\beta}$ where ρ and ρ_0 are resistivities at T and T_0 (characteristic temperature) [30]. For $\beta = 0.25, 0.5$, the transport can be explained by Mott variable-range hopping [31] and Efros–Shklovskii variable-range hopping [32] respectively. According to the fitting, we found that between 20 K to 100 K, β is 0.477, while above 100 K, β is 0.249 which are consistent with Efros–Shklovskii and Mott variable-range hopping models respectively. At temperatures below 20 K, β is 1.035, which can be ascribed to the Arrhenius model. A more detailed study, outside the scope of this work, is needed to fully understand the nature of conduction in our samples. Nonetheless, we can rule out a Dirac semimetal.

To further understand the electronic structure of PdO, we did DFT calculations [33-34] using the HSE exchange-correlation functional, which usually corrects the underestimated bandgap problem with regular exchange-correlation functional, but sometimes can overcorrects (see supplemental materials [35] for details). As can be seen in Fig. 4b (top left), no band inversion is seen and the direct band gap at the M point is as large as ~ 1.0 eV, agreeing with a previous DFT-HSE calculation [36]. This calculated gap is comparable with experimental results from optical measurements, which mostly range from 0.8 eV to 2.6 eV [20-21,37-38]. To reduce the band gap and get band inversion at the M point, we recalculated the band structure by adding strain to the lattice with a Poisson ration of 0.4. According to calculations, a tensile strain along the c -axis is the most effective way to decrease the band gap. Shown in Fig. 4b (top right) is the result by adding 6% tensile strain along c -axis where the gap is $\sim 50\%$ narrower. Upon increasing the tensile strain, the gap is further reduced and finally closed when the tensile strain goes up to 18%. For epitaxial oxide films, strain values of $\sim 2\%$ to $\sim 3\%$ are quite common, and the highest strain of 6.5% was reported in the BiFeO₃ on YAlO₃ (110) substrate [39-40]. However, these values are far

lower than 18%, where band inversion takes place according to our DFT calculation. Thus, it would be a challenge to verify the band inversion in PdO experimentally.

V. Hole Conduction and Post-Annealing in Vacuum

For the as-grown PdO film, we found the Hall slope to be *positive*, as shown in the inset of Fig. 5a. A possible reason for hole carriers in PdO may be due to deficiency of Pd caused by the relatively high O₃ pressure during the growth, though we do not rule out other more intrinsic reasons. Using a single band model, the calculated hole density is $4.02 \times 10^{19}/\text{cm}^3$ at room temperature and increases to $5.97 \times 10^{19}/\text{cm}^3$ at 50 K. Although the carrier density increases by a factor of ~ 1.5 at low temperature, the resistivity increases (Fig. 4a). In *p*-type oxides, localization of doped holes in the valence band has been ascribed to the formation of self-trapping polarons [41], though this possibility has not been investigated in any detail in our samples.

Although the as-grown films show insulating behavior, their resistivity as well as carrier density can be tuned by introducing oxygen vacancies. We systematically investigated a PdO film's structure and transport properties after post-annealing in vacuum ($< 10^{-8}$ Torr) at various temperatures (75 °C, 100 °C, 150 °C and 200 °C) for 30 min each (heating and cooling rate at 20 °C/min). As shown in Fig. 5b, the intensity of PdO (100) and (200) x-ray diffraction peaks decrease upon increasing the annealing temperature and become invisible for temperatures above 150 °C. The corresponding transport properties of the annealed films are shown in Fig. 5c. Compared with the as-grown sample, the film becomes more insulating once annealed at 75 °C and 100 °C. However, further increase of the annealing temperature to 150 °C makes the film very conductive, with metallic behavior at the lowest temperatures. The resistivity decreases even further when the film is annealed at 200 °C.

These behaviors can be explained by considering measurements of Hall resistance shown in Fig. 5d. We propose that for post-annealing at temperatures below 100 °C a relatively small concentration of oxygen vacancies are formed and act as traps for holes. As a result, the net hole density decreases and the film becomes less conductive. When the post-annealing temperature is above 150 °C, more oxygen vacancies are generated and the intensity of the (200) PdO peak disappears as shown in Fig. 5b, implying a collapse of the PdO crystal structure. Electrons now become the dominant carriers and the net carrier density increases by over 100 times at room temperature, reaching $1.79 \times 10^{22}/\text{cm}^3$ and $9.81 \times 10^{22}/\text{cm}^3$ for 150 °C and 200 °C annealing correspondingly, which induces a sharp decrease of resistivity and metallic behavior at low temperatures. A clear sign change of Hall slope can be seen in the inset of Fig. 5d, and the data is measured at 300 K.

VI. Conclusions

In conclusion, using O₃-MBE, we synthesized PdO thin films. In-situ and ex-situ characterization suggest the film is epitaxial to the MgO (001) substrate, with the shorter *a/b* axis oriented out of plane. Contrary to a recent theoretical prediction of a Dirac semimetal, we found that the PdO films are insulating. Using the HSE exchange-correlation functional, we get a ~ 1.0 eV band gap in PdO, and this gap can be reduced effectively by external tensile strain along the *c*-axis. In theory, a topological phase

transition is possible by applying a large external strain along c -axis in PdO. Surprisingly, the predominant carriers in our as-grown PdO films are holes. By gentle vacuum annealing, oxygen vacancies can be introduced into the film, and a transition from a p -type conductor to an n -type metal is realized, accompanied by a gradual structural transformation.

Acknowledgement

We thank Prof. Jian-Min Zuo and Dr. Haw-Wen (university of Illinois Urbana-Champaign) for their assistance with preparation of our PdO films for TEM measurements. We thank Dmitry A. Yarotski from Los Alamos National Laboratory optical measurements. Work at Argonne and Ames is supported by the Center for the Advancement of Topological Semimetals, an Energy Frontier Research Center funded by the U.S. DOE, Office of Basic Energy Sciences. Use of the Center for Nanoscale Materials, an Office of Science user facility, was supported by the U.S. Department of Energy, Office of Science, Office of Basic Energy Sciences, under Contract No. DE-AC02-06CH11357.

- [1] S. M. Young, S. Zaheer, J. C. Y. Teo, C. L. Kane, E. J. Mele, and A. M. Rappe, *Phys. Rev. Lett.* **108**, 140405 (2012).
- [2] S. Murakami, *New J. Phys.* **9**, 356 (2007).
- [3] S. M. Young, S. Chowdhury, E. J. Walter, E. J. Mele, C. L. Kane, and A. M. Rappe, *Phys. Rev. B* **84**, 085106 (2011).
- [4] B. Yan, and C. Felser, *Annu. Rev. Condens. Matter Phys.* **8**, 337 (2017).
- [5] T. Liang, Q. Gibson, M. N. Ali, M. Liu, R. J. Cava and N. P. Ong, *Nat. Mater.* **14**, 280 (2015).
- [6] H. Li, H. He, H.-Z. Lu, H. Zhang, H. Liu, R. Ma, Z. Fan, S.-Q. Shen and J. Wang, *Nat. Comm.* **7**, 10301 (2016).
- [7] S. Nakatsuji, N. Kiyohara and T. Higo, *Nature* **527**, 212 (2015).
- [8] K. Kuroda, T. Tomita, M.-T. Suzuki, C. Bareille, A. A. Nugroho, P. Goswami, M. Ochi, M. Ikhlas, M. Nakayama, S. Akebi, R. Noguchi, R. Ishii, N. Inami, K. Ono, H. Kumigashira, A. Varykhalov, T. Muro, T. Koretsune, R. Arita, S. Shin, T. Kondo and S. Nakatsuji, *Nat. Mater.* **16**, 1090 (2017).
- [9] Y. Sun, Y. Zhang, C. Felser and B. Yan, *Phys. Rev. Lett.* **117**, 146403 (2016).
- [10] M. Kimata, H. Chen, K. Kondou, S. Sugimoto, P. K. Muduli, M. Ikhlas, Y. Omori, T. Tomita, A. H. MacDonald, S. Nakatsuji and Y. Otani, *Nature* **565**, 627 (2019).
- [11] Y. Zhang, Y. Sun, H. Yang, J. Zelezny, S. P. P. Parkin, C. Felser, and B. Yan, *Phys. Rev. B* **95**, 075128 (2017).
- [12] S. S.-L. Zhang, A. A. Burkov, I. Martin, and O. G. Heinonen, *Phys. Rev. Lett.* **123**, 187201 (2019).
- [13] T. Zhang, Y. Jiang, Z. Song, H. Huang, Y. He, Z. Fang, H. Weng, and C. Fang, *Nature* **566**, 475 (2019).
- [14] M. G. Vergniory, L. Elcoro, C. Felser, N. Regnault, B. A. Bernevig, and Z. Wang, *Nature* **566**, 480 (2019).
- [15] F. Tang, H. C. Po, A. Vishwanath and X. Wan, *Nature* **566**, 486 (2019).

- [16] Z. Wang, Y. Sun, X.-Q. Chen, C. Franchini, G. Xu, H. Weng, X. Dai, and Z. Fang, *Phys. Rev. B* **85**, 195320 (2012).
- [17] Z. Wang, H. Weng, Q. Wu, X. Dai, Z. Fang, *Phys. Rev. B* **88**, 125427 (2013).
- [18] P. Hohenberg, W. Kohn, *Phys. Rev.* **136**, 864 (1964).
- [19] W. Kohn, L. J. Sham, *Phys. Rev.* **140**, 1133 (1965).
- [20] A. D. Becke and E. R. Johnson, *J. Chem. Phys.* **124**, 221101 (2006).
- [21] F. Tran and P. Blaha, *Phys. Rev. Lett.* **102**, 226401 (2009).
- [22] D.-J. Yang, I. Kamienski, D. Y. Youn, A. Rothschild, and I.-D. Kim, *Adv. Funct. Mater.* **20**, 4258 (2010).
- [23] J. G. McCarty, *Catal. Today* **26**, 283 (1995).
- [24] H. Okamoto, and T. Aso, *Japan. J. Appl. Phys.* **6**, 779 (1967).
- [25] P. O. Nilsson and M. S. Shivaraman, *J. Phys. C: Solid State Phys.* **12**, 1423 (1979).
- [26] E. Lundgren, J. Gustafson, A. Mikkelsen and J. N. Andersen, *Phys. Rev. Lett.* **92**, 046101 (2004).
- [27] J. Heyd, G. E. Scuseria, and M. Ernzerhof, *J. Chem. Phys.* **124**, 219906 (2006).
- [28] V. Y. Zenou, D. E. Fowler, R. Gautier, S. A. Barnett, K. R. Poepelmeier, L. D. Marks, *Solid State Ionics* **296**, 90 (2016).
- [29] A. L. Patterson, *Phys. Rev.* **56**, 978 (1939).
- [30] R. Rosenbaum, *Phys. Rev. B* **44**, 3599 (1991).
- [31] N. F. Mott, *J. Non-Cryst. Solids* **1**, 1 (1968).
- [32] A. L. Efros and B. I. Shklovskii, *J. Phys. C* **8**, 249 (1975).
- [33] G. Kresse, J. Furthmuller, *Phys Rev B* **54**, 11169 (1996).
- [34] G. Kresse, J. Furthmuller, *Comp. Mater. Sci.* **6**, 15 (1996).
- [35] See Supplemental Material at for further details on DFT calculations, see Ref. [36, 42-45].
- [36] J. A Kurzman, M.-S. Miao and R. Seshadri, *J. Phys.: Condens. Matter* **23**, 465501 (2011).
- [37] R. Ahuja, S. Auluck, B. Johansson and M. A. Khan, *Phys. Rev. B* **50**, 2128 (1994).
- [38] T. Pillo, R. Zimmermann, P. Steiner and S. Hufner, *J. Phys.: Condens. Matter* **9**, 3987 (1997).
- [39] Y. Yang, I. C. Infante, B. Dkhil, L. Bellaiche, *C. R. Physique* **16**, 193-203 (2015).
- [40] A. Biswas and Y. H. Jeong, *Epitaxy*, Miao Zhong, IntechOpen, DOI: 10.5772/intechopen.70152.
- [41] J. B. Varley, A. Janotti, C. Franchini and C. G. van de Walle, *Phys. Rev. B* **85**, 081109(R) (2012).
- [42] P. E. Blöchl, *Phys. Rev. B* **50**, 17953-17979 (1994).
- [43] J. Heyd, G. E. Scuseria, M. Ernzerhof, *J. Chem. Phys.* **118**, 8207-8215 (2003).
- [44] H. J. Monkhorst, J. D. Pack, *Phys. Rev. B* **13**, 5188-5192 (1976).
- [45] J. A. Kurzman, M.-S. Miao, R. Seshadri, *J. Phys.: Condens. Matter* **23**, 465501 (2011).

Fig. 1

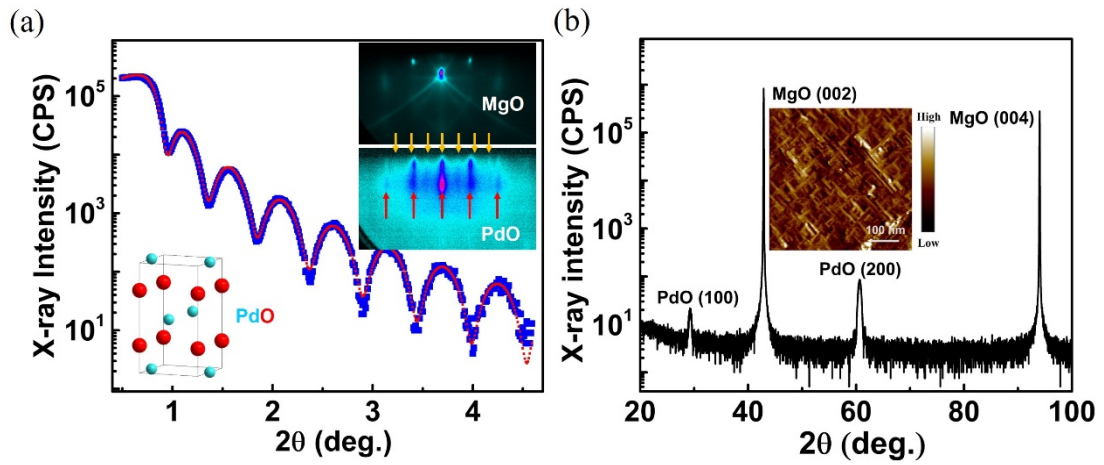


Fig. 1 (a) X-ray reflectivity of PdO film (blue and red curves are the measured data and fitting respectively). Bottom Inset: crystal structure of tetragonal PdO where blue and red atoms are Pd and O respectively; Top inset: RHEED image before and after PdO growth. Yellow and red arrows are used to indicate two sets of streaks. The spacing ratio is ~ 1.77 corresponding to c/a . (b) X-ray diffraction of PdO. Inset: AFM image of the film. Scale bar ranges 100 nm. The edges of AFM image are parallel to the $[100] / [010]$ of MgO.

Fig. 2

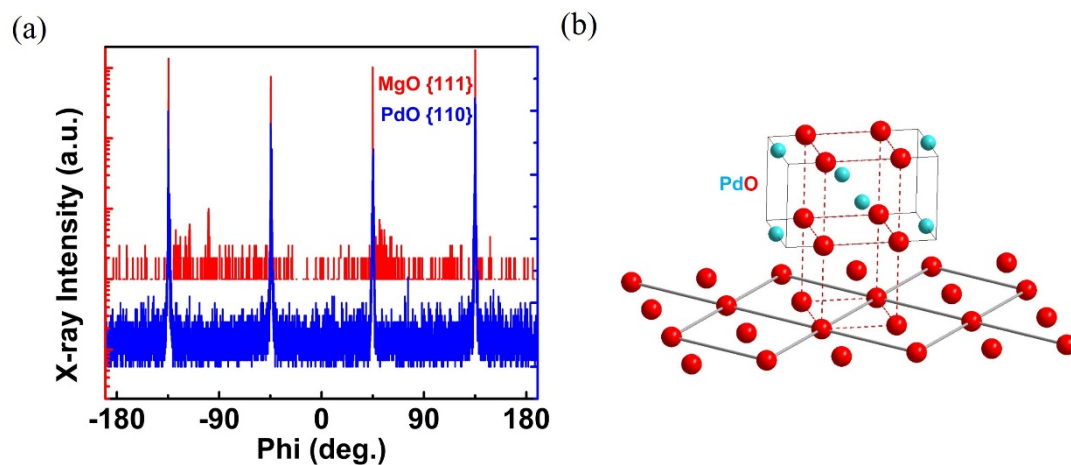


Fig. 2 (a) X-ray Phi scan along MgO {111} and PdO {110}, and the 4-fold symmetry in PdO indicate the film is twinned. (b) schematics of epitaxial relation between PdO (100) / (010) and MgO (001). For rock salt structure in MgO, only O atoms are shown for simplicity.

Fig. 3

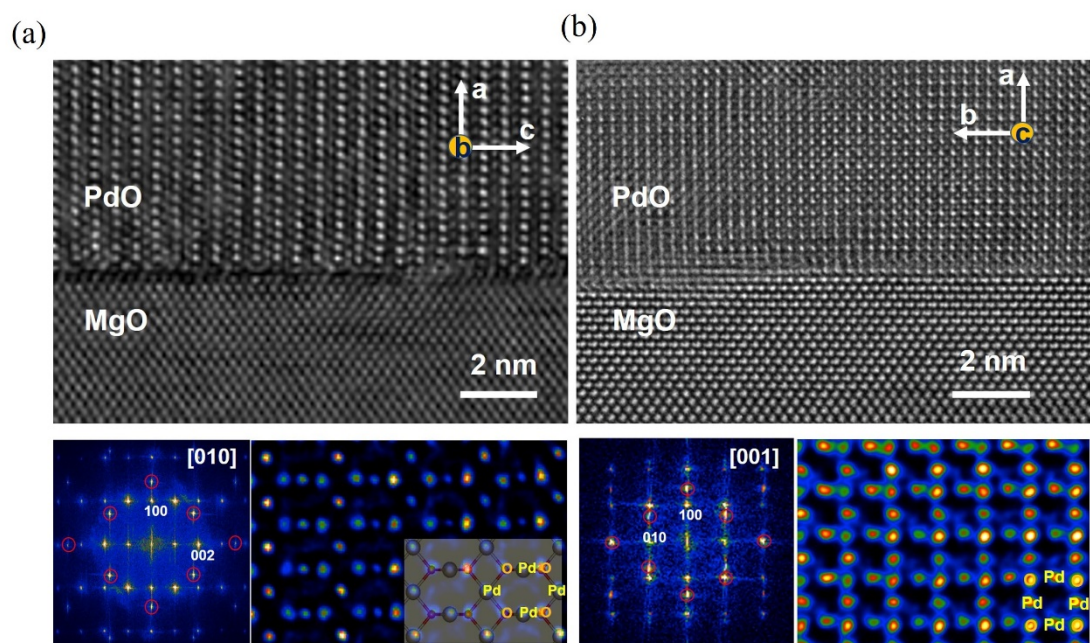


Fig. 3 High resolution TEM images and FFT patterns of PdO / MgO sample viewed along MgO [110]. Two sets of atomic structures are seen where (a) is along [010] and (b) is along [001] of PdO. Bottom panels of each figure are reciprocal pattern of selected area (left) and reconstructed atomic structure (right).

Fig. 4

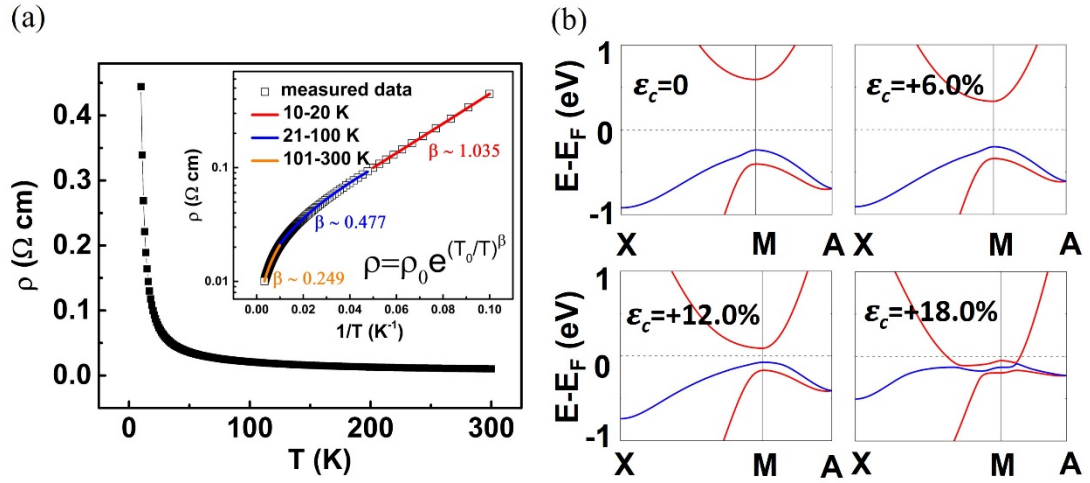


Fig. 4 (a) Temperature dependence of PdO resistivity in our film. Inset: fitting of the measured data using hopping law expression. (b) Band gap evolution of PdO applying HSE exchange-correlation functional under $\varepsilon_c=0$ (top left), +6% (top right), +12% (bottom left) and +18% (bottom right) tensile strain along c axis.

Fig. 5

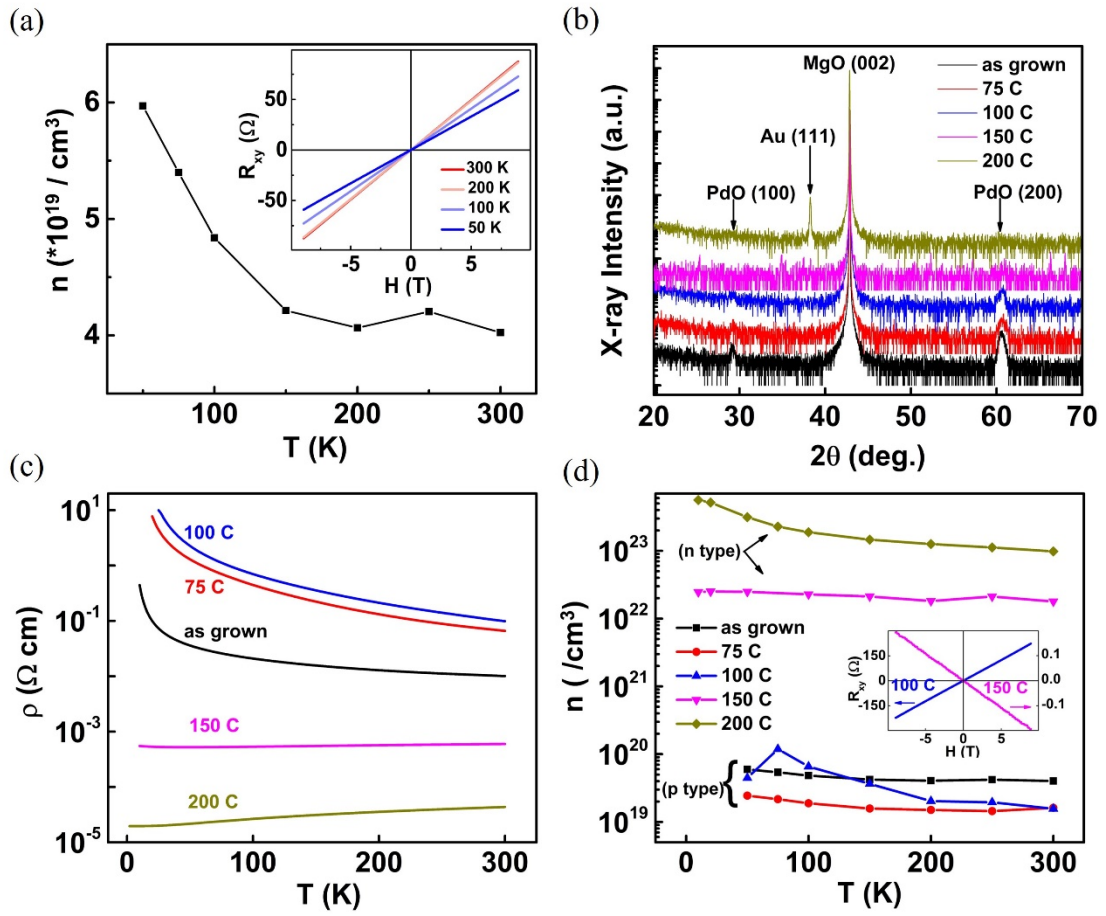


Fig. 5 (a) Temperature dependence of carrier density of as-grown PdO film. Inset: magnetic field dependence of Hall resistance at various temperatures. (b) X-ray diffraction and (c) temperature dependent resistivity of PdO film after growth and post-annealing at various temperatures. (d) Temperature dependences of carrier densities in reduced PdO films. Inset: field dependence of Hall resistivities at 300 K for 100 °C and 150 °C annealed films where a sign change of slope can be clearly seen.